Journal of Alloys and Compounds 512 (2012) 171–178

Contents lists available at SciVerse ScienceDirect

Journal of Alloys and Compounds

journal homepage: www.elsevier.com/locate/jallcom

Sol–gel derived Li–Mg co-doped ZnO films: Preparation and characterization via XRD, XPS, FESEM

Seval Aksoy*, Yasemin Caglar, Saliha Ilican, Mujdat Caglar

Anadolu University, Faculty of Sciences, Department of Physics, Eskisehir, 26470, Turkey

ARTICLE INFO

Article history:
Received 25 July 2011
Received in revised form
15 September 2011
Accepted 19 September 2011
Available online 24 September 2011

Keywords:
Li and Mg co-doping
ZnO
Sol–gel
Dispersion parameters
XPS

ABSTRACT

Li–Mg co-doped ZnO films have been deposited onto glass substrates by sol–gel spin coating method. The structural and morphological properties of the films were characterized by X-ray diffractometer (XRD), X-ray photo-electron spectroscopy (XPS) and field emission scanning electron microscopy (FESEM). The XRD spectra indicated that the films have polycrystalline nature. The crystallite size values decreased with the increasing Mg content. The chemical composition of the Li–Mg co-doped ZnO films were confirmed by XPS. Additionally, XPS results clearly showed the existence of Mg as a doping element into ZnO crystal lattice. The surface morphology of the films was found to depend on the concentration of Mg in the ZnO:Li. The absorption band edge values of the films were calculated and these values of the films increased with increasing Mg concentration. The refractive index dispersion curves of the films obeyed the single-oscillator model. The dispersion parameters such as E_o (single-oscillator energy) and E_d (dispersive energy) of the films were determined and increase with Mg content.

1. Introduction

The important properties of nanostructured materials have started motivation among scientists to explore the possibilities of using them in technological applications. In particular, the electronic and optical properties of nanostructured materials have been of interest because of their potential applications in the fabrication of micro electronic and optoelectronic devices [1,2].

Zinc oxide (ZnO) with a wide band gap (3.37 eV) n-type semiconductor and high exciton binding energy (60 meV) at room temperature is attractive for optoelectronic applications in the blue and UV regions, e.g., light emitting diodes and laser diodes. A lot of attention has been paid to the fabrication the ZnO film. Among them, RF magnetron sputtering [3], chemical vapor deposition (CVD) [4], pulsed laser deposition [5], photo-atomic layer deposition [6], metal oxide chemical vapor deposition [7], molecular beam epitaxy [8], filtered cathodic vacuum arc method [9] and sol–gel method [10] are the most commonly used methods. Sol–gel process is an attractive method for obtaining films because it has advantages of easy control of the film composition and easy fabrication of large-area films with low cost. Most of the experimental investigations related to the co-doping materials, such as Ga–N [3], In–N [4] and Al–N [11], have also appeared in several literatures, and moreover the p-type behavior in co-doped ZnO is demonstrated an acceptable stability [11].

The doping of Li or Mg into ZnO films could improve their preferential orientation growth, but it was sensitive to a heating procedure. Usually, high heat treatment temperature leads to good preferential orientation and large crystallite size; contrarily, low temperature favors random orientation and small crystallite size [9]. Some physical properties of Li and Mg co-doped ZnO films were reported by some previous work. Fujihara et al. [12] prepared Li and Mg co-doped ZnO films by the sol–gel method. After then, effects of doping on microstructure and electrical properties were examined. They found that the ZnO crystallite size increased by doping and the surface of the films became rougher. Also, the current density of the films was reduced by doping probably due to the formation of acceptor levels (Li-doping) and the reduction of oxygen defects (Mg doping). The film with a nominal composition of $Zn_{0.85}Li_{0.10}Mg_{0.05}O$ showed the lowest current density of 1.7×10^{-6} A cm^{-2} in this study. Liu et al. [13] prepared Li and Mg-doped ZnO films on glass substrates by sol–gel method and two-step growth. They found that Mg doping into Li:ZnO films improved c-axis orientation and increased the resistivity. Highly c-axis orientation, small crystallite size and high resistivity were found for the (Li, Mg): ZnO film with Li/Zn molar ratio of 0.10 and Mg/Zn molar ratio of 0.04 by the two-step growth at 550 °C for 1st spinning and 500 °C for 2nd spinning. Zhu et al. [14] prepared the ZnO nanorods on glass substrate by doping Li^+ and/or Mg^{2+} using a sol–gel method. The results showed that the degree of c-orientation of Li/Mg doped ZnO nanorods was much high compared with that of Li doped and

* Corresponding author. Tel.: +90 222 3350580; fax: +90 222 3204910.
E-mail address: sevala@anadolu.edu.tr (S. Aksoy).

0925-8388/$ – see front matter © 2011 Elsevier B.V. All rights reserved.
doi:10.1016/j.jallcom.2011.09.058

undoped ones. The authors expressed that Li^+ diffused into the ZnO lattice and occupied the site of Zn^{2+} during the heat-treatment. Unlike us, Chen et al. [15] prepared Li doped ZnMgO (ZnMgO:Li) films via dc reactive magnetron sputtering followed by a thermal anneal process. Firstly, ZnMgO films were prepared on glass substrates by dc reactive magnetron sputtering. Ternary Zn_xMg_{1-x}:Li alloys (x = 0.04, 0.16), doped with 0.1 at.% Li, were used as the targets for fabricating the Li monodoped ZnMgO films. The conductivity of Li-doped films were transformed from highly resistant to p-type via anneal.

In this study, Li and Mg co-doped ZnO films have been fabricated on glass substrates by the sol–gel process and effects of the doping on the structural, morphological and optical properties of the films have been investigated. The chemical properties of the films have been also investigated by X-ray photoelectron spectroscopy (XPS).

2. Experimental detail

Li–Mg co-doped ZnO films have been deposited by sol–gel spin coating method onto glass substrates. As a starting material and dopant source, zinc acetate dihydrate [$Zn(CH_3COO)_2{\cdot}H_2O$] (ZnAc), lithium chloride [LiCl] (LC) and magnesium chloride hexahydrate [$MgCl_2{\cdot}6H_2O$] (MgCl) were used. 2-Methoxethanol ($C_3H_8O_2$) and monoethanolamine (C_2H_7NO, MEA) were used as a solvent and stabilizer, respectively. The molar ratios of MEA to ZnAc, MEA to LC and MEA to MgCl were maintained at 1:1. The concentration of these solutions was 0.5 M. Films with MgCl/ZnAc nominal volume ratio of 2%, 4%, 6% and 8% under a constant LiCl/ZnAc nominal volume ratio of 10% were prepared two step. The solutions were stirred at 60 °C for 2 h to yield a clear and homogeneous solution. The coating solution was dropped into a glass substrate, which was rotated at 3000 rpm for 30 s using a spin coater. After depositing by spin coating, the films were dried at 300 °C for 10 min in a furnace to evaporate the solvent and remove organic residuals. The procedures from coating to drying were repeated 10 times. The films were then inserted into a tube furnace and annealed in air at 500 °C for 1 h. The thickness of the films were determined with Mettler Toledo MX5 microbalance by using weighing method and found to be almost 700 nm.

X-ray diffraction patterns were obtained with a BRUKER D8 Advance X-ray diffractometer using the *CuKα* radiations (λ = 1.54059 Å) and data in the angular region of 2θ = 30–60° were collected at room temperature in a step-scanning mode, with a step length of 0.02°. XPS (SPECS) was used to determine the surface chemical composition of the films using *AlKα* X-rays and the presented bonding states. Surface morphology was studied using a ZEISS Ultraplus model field emission scanning electron microscopy (FESEM). For the transmittance and reflectance measurements, we used a double beam Shimadzu 2450 UV-spectrophotometer with an integrating sphere in the wavelength range 190–900 nm.

3. Results and discussion

3.1. Structural and morphological properties

The XRD patterns of the Li–Mg co-doped ZnO films are shown in Fig. 1. The strongest diffraction peak for all the films was (0 0 2) line. The (0 0 2) peak values of the LMZ2 (10% Li-doped ZnO:2%Mg), LMZ4 (% Li-doped ZnO:4%Mg), LMZ6 (% Li-doped ZnO:6%Mg) and LMZ8 (% Li-doped ZnO:8%Mg) were found to be 34.403, 34.389, 34.433 and 34.403, respectively. The planes of the hexagonal ZnO crystal structure correspond to the (1 0 0), (0 0 2), (1 0 1) Miller indices (Fig. 1). No other phases such as Li, Mg and their oxides can be detected in the films. The reason for this may be no significant amount of dopant concentration that is incorporated in the film. Similar results were reported by Yu et al. [16] and Wang et al. [17]. The crystalline structures of the films are shown depending on the increasing of magnesium content in Fig. 1. With increasing Mg content the intensity of the (0 0 2) peak decreases gradually and FWHM values of this peak broaden. So, the crystalline structure tends to deteriorate due to the substitution of Mg by Zn. The deterioration of the structure depending on the doping in ZnO is usually an expected result [17–20]. In our previous studies, ZnO doped with different element such as F, Sn, Mn, Cd and In [21–24], we also observed similar behaviors. Above metals which have different ionic radius deteriorate the crystalline structure. However, Li^+ ions incorporated into ZnO improve the crystalline structure

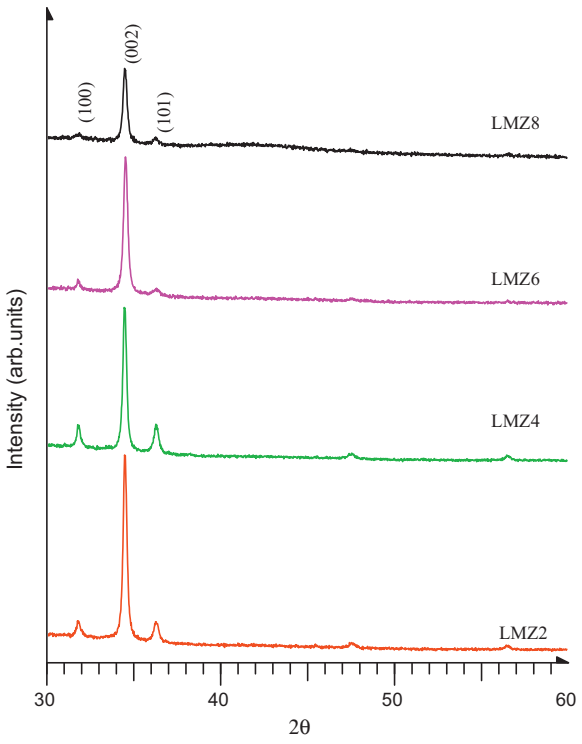

Fig. 1. XRD patterns of the Li–Mg co-doped ZnO films.

[25]. This result can be considered that heterogeneous nucleation is facilitated in the presence of Li^+ ions in the ZnO structure.

The angle of diffraction (2θ), full width half maximum values (*FWHM*) and the phases identified along with *(h k l)* planes of the films are presented in Table 1. *TC* value represents the texture of the particular plane, deviation of which from unity implies the preferred growth. The different texture coefficient *TC(h k l)* have been calculated from the X-ray data using the formula [26]:

$$TC(h\ k\ l) = \frac{I(h\,k\,l)/I_o(h\,k\,l)}{N^{-1}\sum_n I(h\,k\,l)/I_o(h\,k\,l)} \quad (1)$$

where *I(h k l)* is the measured relative intensity of a plane *(h k l)*, $I_o(h\,k\,l)$ is the standard intensity of the plane *(h k l)* taken from the JCPDS data, *N* is the reflection number and *n* is the number of diffraction peaks. The texture coefficient (*TC*) values are presented in Table 1. It can be seen that the highest *TC* is in (0 0 2) plane for all the films. As seen this table, while *TC*(0 0 2) values decrease with increasing Mg content.

A perfect crystal would extend infinitely in all directions; therefore, no crystals are perfect due to their finite size. This deviation from perfect crystallinity leads to a broadening of the diffraction peaks. The two main properties extracted from peak width analysis are the crystallite size and lattice strain. Crystallite size and lattice strain affect the Bragg peak in different ways. Both these effects increase the peak width and intensity and shift the 2θ peak position accordingly [27]. To estimate the average crystallite size of the films Scherrer's formula [28] was used:

$$D = \frac{0.9\lambda}{\beta\cos\theta} \quad (2)$$

where *D* is the average crystallite size of the films, λ (=1.5405 Å) the wavelength of X-rays used, β the broadening of diffraction line measured at half its maximum intensity in radians and θ is the angle of diffraction. The crystallite size values for the LMZ2, LMZ4, LMZ6 and LMZ8 films are found to be 41.2, 42.4, 36.5 and 30.4 nm, respectively. The crystallite size decreases with the increase of Mg

Table 1
Structural parameters of the Li–Mg co-doped ZnO films.

(h k l)	LMZ2			LMZ4			LMZ6			LMZ8		
	2θ	FWHM	TC	2θ	FWHM	TC	2θ	FWHM	TC	2θ	FWHM	TC
100	31.703	0.224	0.59	31.712	0.185	0.73	31.707	0.081	0.57	31.684	0.149	0.53
002	34.403	0.211	3.35	34.389	0.205	2.94	34.433	0.238	2.73	34.403	0.286	1.69
101	36.197	0.324	0.60	36.206	0.271	0.80	36.221	0.428	0.42	36.164	0.248	0.52

content. This confirms the deterioration in the crystallinity of the films. This effect can be explained if it is considered that magnesium atoms do not substitute oxygen atoms, instead they occupy interstitial sites resulting in a large number of dislocations.

The strain of the films was calculated using Williamson–Hall (W–H) method. The W–H approach considers the case when the domain effect and lattice deformation are both simultaneously operative and their combined effects give the final line broadening FWHM (β), which is the sum of (D) (grain size) and β (lattice distortion). This relation assumes a negligibly small instrumental contribution compared to the sample-dependent broadening. W–H equation may be expressed in the form [29]:

$$\beta\cos\theta = \frac{k\lambda}{D} + 4\varepsilon\sin\theta \quad (3)$$

where ε is the strain associated with the nanoparticles. Eq. (3) represents a straight line between $4\sin\theta$ (X-axis) and $\beta\cos\theta$ (Y-axis). The slope of line gives the strain (ε). Lattice strain is a measure of the distribution of lattice constants arising from crystal imperfections, such as lattice dislocations. The strain values for the LMZ2, LMZ4, LMZ6 and LMZ8 films are found to be 9.6×10^{-3}, 8.8×10^{-3}, 37.3×10^{-3} and 12×10^{-3}, respectively.

XPS spectroscopy is a material characterization technique widely used to investigate the chemical composition of materials. The technique is based on collecting the electrons that are ejected from atoms of the sample being analyzed when irradiated by X-rays. The X-ray photons do not cause any structural damage to the sample and only those photoelectrons that escape the material without undergoing inelastic scattering are used in the analysis. The technique is non destructive and highly surface sensitive. XPS provides compositional analysis of approximately the top 5 nm of material below the studied samples surface. In this study, in order to estimate the contained Mg concentration in the films and to determine the chemical states of the film composing elements, XPS analysis were carried out for LMZ2 and LMZ8 films and the energy scale was calibrated with the C1s peak of the carbon contamination at 284.60 eV. The atomic ratio of Mg/ZnO:Li in this samples have been also calculated from the XPS survey spectra to be about 0.0164 and 0.0774 for LMZ2 and LMZ8 films, respectively. These values are very close to their nominal volume ratios. The binding states of O1s spectra belonging to LMZ2 and LMZ8 films are shown in Fig. 2. XPS peak of O1s shows the apparent asymmetry. This peak could be divided into three nearly Gaussian components: which are low binding energy peak, middle binding energy peak and high binding energy peak centered around 530.17 eV, 530.42 eV and 532.17 eV for LMZ2 film, and 529.55 eV, 530.37 eV and 532.15 eV for LMZ8 film, respectively. The low binding energy peak of the O1*s* spectrum can be attributed to the O^{2-} ions on the wurtzite structure of the hexagonal Zn^{2+} ion array, which are surrounded by zinc atoms with the full supplement of nearest-neighbor O^{2-} ions [30,31]. The component at the medium binding energy of the O1*s* peak is associated with O^{2-} ions that are in oxygen-deficient regions within the ZnO matrix [31]. The high binding energy component can be attributed to the presence of loosely bound oxygen on the surface of ZnO nanocystals [31,32]. Figs. 3 and 4 give the XPS data of Zn2p3/2 and Zn2p1/2 for LMZ2 and LMZ8 films, respectively. The Zn2p3/2 spectra peaked at 1021.70 eV and 1021.80 eV can be attributed to the binding energy of Zn–O bond rather than metallic Zn because the binding energy of Zn–O bond (1021.90 eV) is higher than that of the Zn–Zn bond (1021.45 eV) [33,34]. The binding energy of Zn2p1/2 peak for LMZ2 and LMZ8 films is observed at 1044.80 eV [34]. This peak can be attributed to binding energy of Zn–O bond (1044.78 eV) [35]. The Mg1s peak is shown in Fig. 5 with the metallic and oxide components deconvoluted. Mg1s peak presents two components at 1303.06 eV and 1303.95 eV for LMZ2 and 1303.48 eV and 1304.85 eV for LMZ8 film, respectively. The peaks at 1303.06 eV and 1303.48 eV represent metallic magnesium for LMZ2 and LMZ8 films and also the peaks at 1303.95 eV and 1304.85 eV show clearly

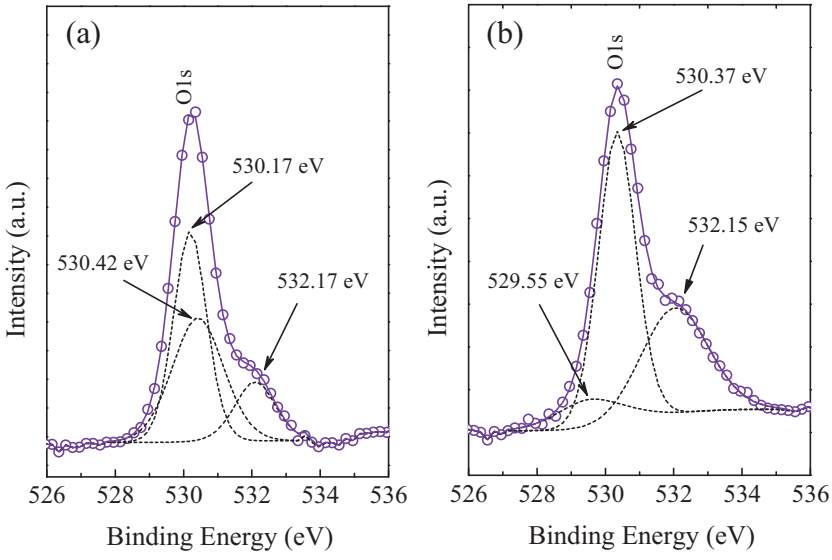

Fig. 2. XPS spectra (open circles) and simulated lines of O1s in the (a) LMZ2 film and (b) LMZ8 film.

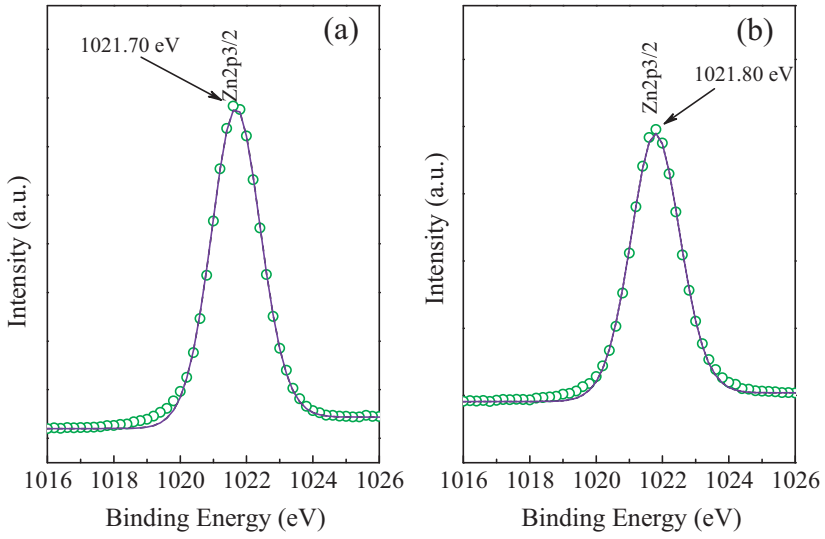

Fig. 3. XPS spectra (open circles) and simulated lines of Zn2p3/2 in the (a) LMZ2 film and (b) LMZ8 film.

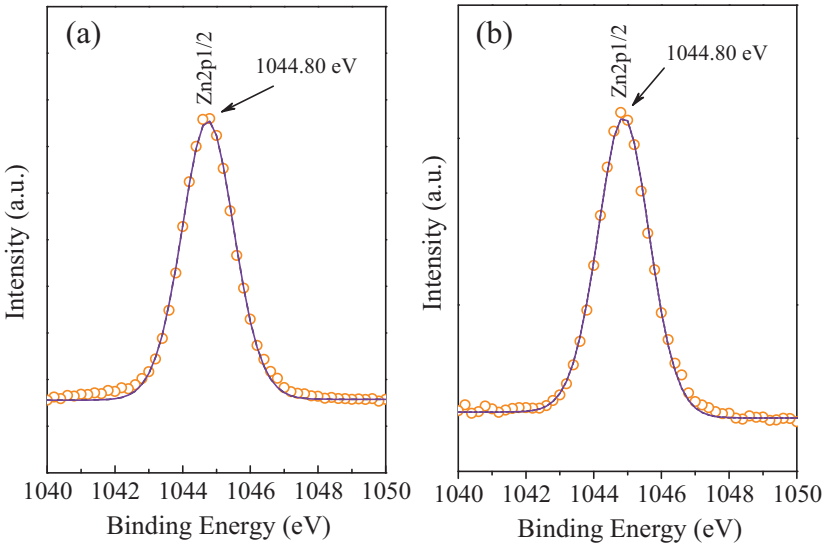

Fig. 4. XPS spectra (open circles) and simulated lines of Zn2p1/2 in the (a) LMZ2 film and (b) LMZ8 film.

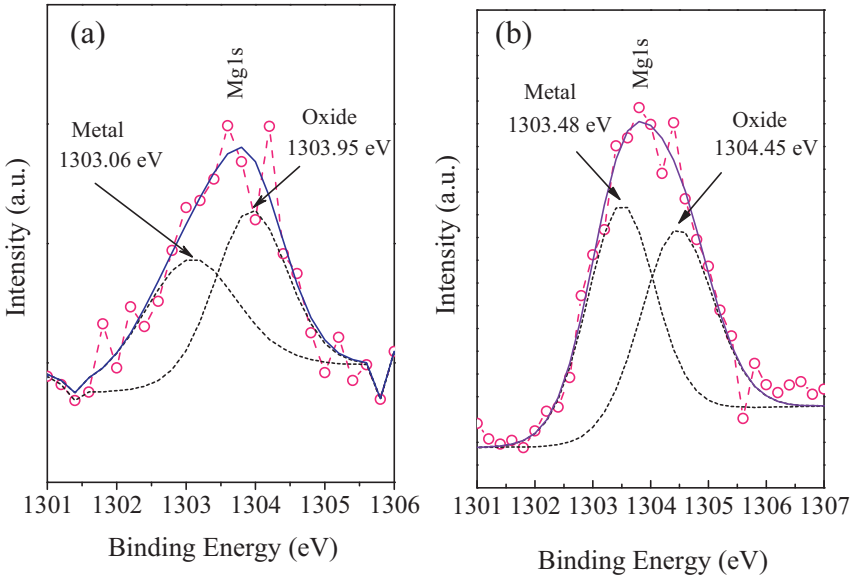

Fig. 5. XPS spectra (open circles) and simulated lines of Mg1s in the (a) LMZ2 film and (b) LMZ8 film.

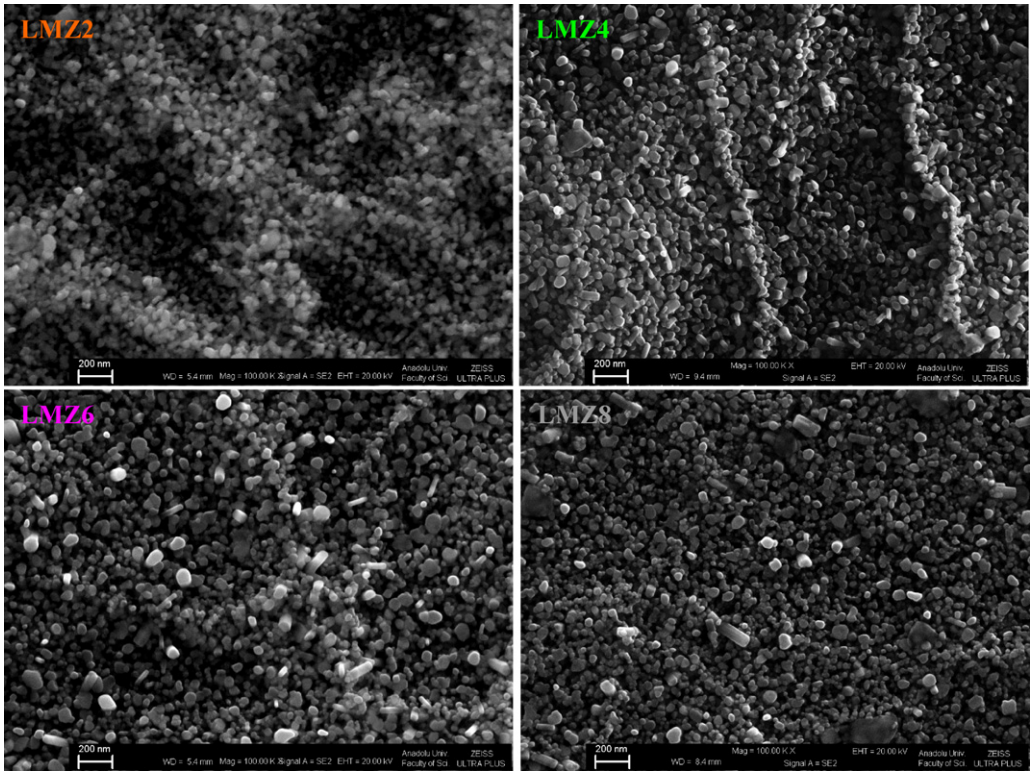

Fig. 6. FESEM images of the Li–Mg co-doped ZnO films.

the presence of MgO [36]. However, a peak corresponding to the lithium element has not been detected in XPS survey spectrums. It may be due to a small amount of Li element into ZnO crystal lattice or the detection limit of XPS [15,37].

The surface morphological properties of the films were analyzed using FESEM. Fig. 6 shows FESEM images of the all the films. In general ZnO films produced by sol–gel method show a wrinkle network with spherical nano-sized crystallites on the surface [22,24,25]. Sometimes these surface properties of ZnO are influenced from the incorporation of dopant. Especially the amount and kind of dopant can play an important role on the surface properties. For example, in the Sn doped ZnO films the tetragonal shape particles were appeared on the surface with Sn doping [22]. The wrinkle structure was disappeared with increasing Li content [25]. Only for 10%F doped ZnO, the randomly oriented nanorods with diameter in the range 50–100 nm were observed on the surface [21]. The surface quality of the ZnO film improved with Mn doping, because the incorporation of the Mn ions gave the regular grain size. The regular grain size caused the more uniform film. In this study, it can be clearly observed that the surface morphology of the films changed with Mg concentration. When the surface morphologies of the films are examined, non-uniform particle distribution is observed on the surface while increasing Mg concentration. The rod-like crystallites separately grown on the substrate can also be seen depending on increasing Mg content. The randomly distributed nanorods are shown in Fig. 6 (b–d). This situation indicating that increasing Mg concentration can substantially enhance the growth of nanorods.

3.2. Optical properties

The spectral distribution of transmittance (T) and reflectance (R) measured in the wavelength range 350–700 nm for the films are shown in Figs. 7 and 8, respectively. The average transmittance is found to be almost 80% for the visible region. As seen inset in Fig. 7, the absorption edge shifts toward shorter wavelengths with increasing Mg content. As seen in Fig. 8, the reflectance is limited only by the surface reflectance of about 10% in the visible region.

The absorption coefficient (α) is related to the energy band gap (E_g) as [38]:

$$\alpha = \frac{A}{h\nu}(hn - E_g)^n \tag{4}$$

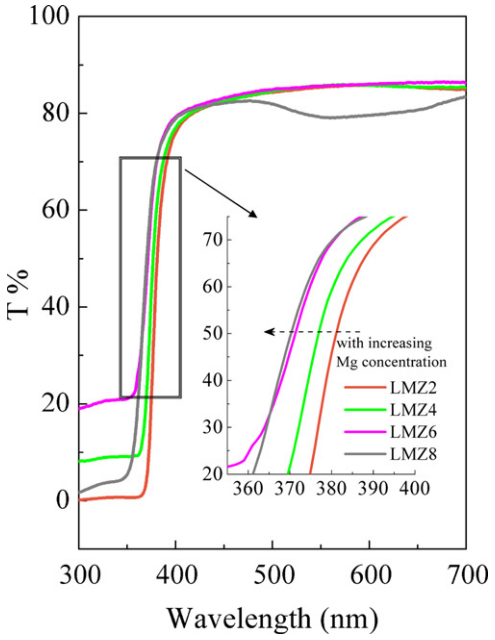

Fig. 7. The transmittance spectra of the Li–Mg co-doped ZnO films.

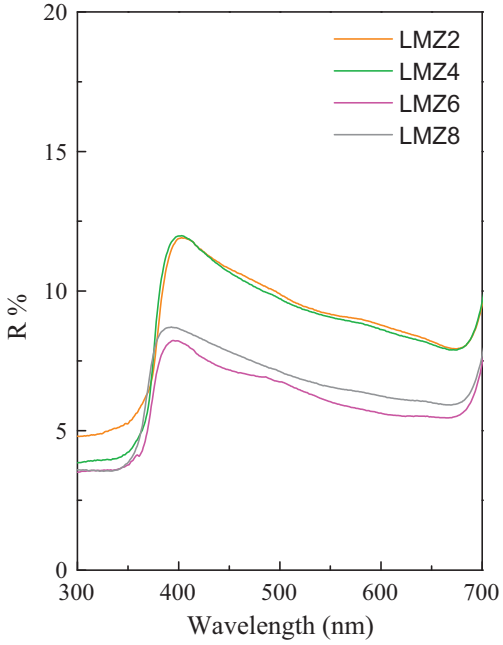

Fig. 8. The reflectance spectra of the Li–Mg co-doped ZnO films.

where '*A*' is a constant dependent on the material, '*h*', and 'ν' are the Planck constant and frequency of the radiation, respectively. The nature of the transition is represented by '*n*'. For allowed direct and indirect transitions, the values of '*n*' are 1/2 and 2, respectively. The corresponding values for forbidden transitions are 3/2 and 3, respectively. The value of '*n*' can be determined from the slope of $\ln(\alpha h\nu)$ vs. $\ln(h\nu - E_g)$ plots. With linear fitting of the plot gives the value of '*n*', for the films, which is close to 0.5. It is known as the allowed direct transition [38].

To estimate the energy band gap of the films, the first derivative curve of the optical transmittance ($dT/d\lambda$) presented in Fig. 7 can be computed. These derivative curves in the wavelength range of interest are presented in Fig. 9. The peak value in each curve is associated to the optical band-gap energy E_g [39], where it is calculated using the following equation:

$$E_g = \frac{hc}{\lambda_{max}} \tag{5}$$

where h is the Planck constant, c is the light velocity and λ_{max} is the wavelength in the maximum of the derivative curve. The E_g values are determined using Eq. (5), where λ_{max} is obtained by a least square fitting procedure of the parable. As seen in Fig. 9, the peak

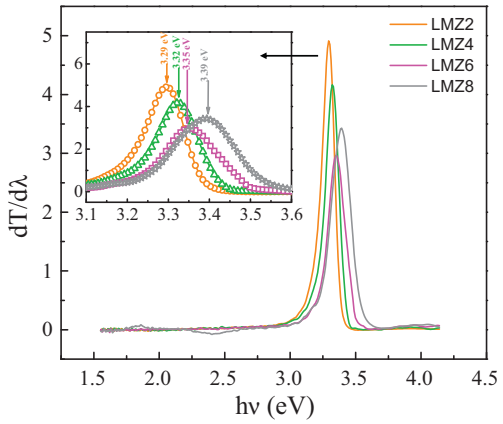

Fig. 9. The plots of $dT/d\lambda$ vs. photon energy of the Li–Mg co-doped ZnO films.

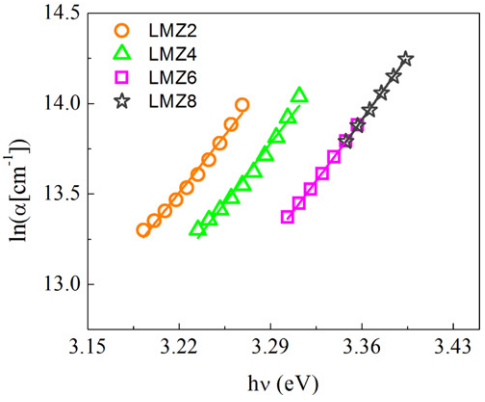

Fig. 10. The Urbach plot of the Li–Mg co-doped ZnO films.

position of the curves shifts to higher energies with Mg concentration. The absorption band edge values are given inset in Fig. 9. This suggests that the absorption band edge shifts from 3.29 eV to 3.39 eV with Mg concentration. The peak point of the derivative spectra could be regarded as the approximate optical band gap value. This blue shift in the optical band gap of the films may be attributed to the band Burstein–Moss effect. The increase of carrier concentration in doped film will cause the Fermi level move into the conduction band. The filling of the conduction band by electrons will generally result in blue shift in the near band edge emission.

The width of the localized states in the optical band gap of the films that result from crystal defects like vacancies, interstitial atoms, and atoms at surfaces and grain boundaries affects the optical band gap structure and optical transitions and it is called as Urbach tail, which is related directly to a similar exponential tail for the density of states of either one of the two band edges [40]. The Urbach tail of the films can be determined by the following relation [41]:

$$\alpha = \alpha_0 \exp\left(\frac{E}{E_U}\right) \tag{6}$$

where E is the photon energy, α_0 is constant and E_U is the Urbach energy which refers the width of the exponential absorption edge. In summary, Eq. (6) describes the optical transition between occupied states in the valence band tail to unoccupied states of the conduction band edge. Fig. 10 shows the variation of $\ln\alpha$ vs. photon energy for the films. This behavior corresponds primarily to optical transitions between occupied states in the valence band tail and unoccupied states at the conduction band edge. The E_U value was calculated from the slope of Fig. 10 using relationship:

$$E_U = \left(\frac{d(\ln \alpha)}{d(h\nu)}\right)^{-1} \tag{7}$$

The obtained E_U values are given in Table 2. Urbach energy values of the films decrease with increasing Mg concentration. ZnO has native defects such as oxygen vacancies and interstitial zinc atoms. So, the additional dopant may dominantly contribute to the width of localized states within the optical band of ZnO. Hence, the E_U values change inversely with optical band gaps of the films. Every dopant does not show same effect on the optical properties

Table 2
The optical parameters of the Li–Mg co-doped ZnO films.

	E_U (meV)	β	E_o (eV)	E_d (eV)	M_{-1}	M_{-3} (eV)$^{-2}$
LMZ2	110	0.233	4.863	9.564	1.967	0.083
LMZ4	106	0.241	4.879	9.623	1.972	0.083
LMZ6	104	0.245	6.063	10.057	1.659	0.045
LMZ8	100	0.256	6.092	10.658	1.749	0.047

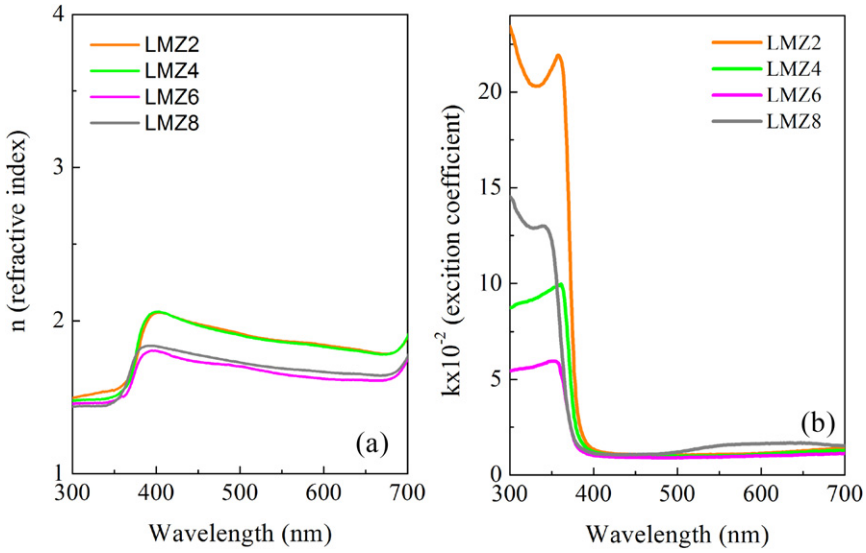

Fig. 11. The variation of refractive index (a) and extinction coefficient (b) of the Li–Mg co-doped ZnO films.

of the ZnO films. While some dopant elements cause an increase in the optical band gap, some of them cause a decrease. For example Li dopant increases the band gap like Mg [25]. However, some dopants such as Sn, Mn, Cd and In cause a decrease in the optical band gap of ZnO [22–24,42].

The dependence of the optical absorption coefficient on photon energy arises from electronic transitions between localized states. The density of these states falls off exponentially with energy which is consistent the theory of Tauc [43]. Therefore, Eq. (6) can be rewritten as:

$$\alpha = \alpha_0 \exp\left[\frac{\beta}{kT}E\right] \tag{8}$$

where β is called a steepness parameter, which characterizes the broadening of the absorption edge due to the electron–phonon interaction or exciton–phonon interaction. The β parameter is found as $\beta = kT/E_U$. The β values were calculated using this relationship and taking $T = 300$ K and are given in Table 2. The β values increase with the increasing Mg concentration.

The refractive index is an important parameter for optical materials and applications. Thus, it is important to determine optical constants of the films and the complex optical refractive index of the films are described by the following relation [44],

$$\widehat{n} = n(\omega) + ik(\omega) \tag{9}$$

where n is the real part and k is the imaginary part (extinction coefficient) of complex refractive index. The refractive index of the films was determined from the following relation [45],

$$n = \left(\frac{1+R}{1-R}\right) + \sqrt{\frac{4R}{(1-R)^2} - k^2} \tag{10}$$

where k ($k = \alpha\lambda/4\pi$) is the extinction coefficient. The n and k values dependence of photon energy are shown in Fig. 11a and b, respectively. The change in the refractive index is a result of the Mg concentration. The trend of lowering of refractive index with doping incorporation can be attributed to the density and the surface roughness [23,24].

The refractive index is a significant factor in optical communication and in designing devices for spectral dispersion and the refractive index dispersion data below the interband absorption edge are important for technological applications of the optical materials, because, the dispersion energy is related to the optical transition strengths and optical conductivity. Thus, in order to analyze the refractive index dispersion of the films, we used the single-oscillator model, developed by DiDomenico and Wemple [46]. In terms of the dispersion energy E_d and single-oscillator energy E_o, the refractive index at a frequency can be expressed. The single-oscillator model for the refractive index dispersion is expressed as follows [46]:

$$n^2 = 1 + \frac{E_d E_o}{E_o^2 - (h\nu)^2} \tag{11}$$

where n is the refractive index, and E_o is the single-oscillator energy for electronic transitions and E_d is the dispersion energy which is a measure of the strength of interband optical transitions. This model describes the dielectric response for transitions below the optical gap. The plotted $(n^2-1)^{-1}$ vs. $(h\nu)^2$ allows us to determine the oscillator parameters. E_o and E_d values were calculated from this plot. The E_o and E_d values are given in Table 2. It was found that oscillator parameters are of the same order as a number of materials [47,48]. E_d and E_o values for ZnO are 17.1 and 6.4 [49]. In generally, E_d and E_o values decrease with dopant incorporation [21,50,51] and this lowering can be attributed to the microstructure that changes with doping.

On the other hand, the parameters of the single-oscillator model E_o and E_d are connected to M_{-1} and M_{-3} moments of the optical spectra, through the two relations [52]:

$$E_o^2 = \frac{M_{-1}}{M_{-3}}, \qquad E_d^2 = \frac{M_{-1}^3}{M_{-3}} \tag{12}$$

The two moments M_{-1} and M_{-3} were calculated from the data on E_o and E_d are given in Table 2. The obtained M_{-1} and M_{-3} moments change with Mg content. These moments are the measure of the average bond strength. Eq. (12) indicates a single oscillator approximation to the dielectric response of these materials. The optical moments are related to the macroscopic quantities like effective dielectric constant, effective number of valence electrons in material investigated.

4. Conclusions

In summary, Li–Mg co-doped ZnO films were deposited by sol–gel method using spin coating method. The structural, morphological and optical properties of these films have been investigated. The films showed a preferential orientation along (*002*) crystal

plane. It was observed that the surface exhibited changes with increasing Mg concentration. The average transmittance of the films was found to be almost 80% for the visible region. The absorption band edge values of the films increased with increasing Mg concentration. The blue shift in the optical band gap of the films was attributed to the band Burstein–Moss effect. Urbach energy of the films changed with optical band gap. The refractive index dispersion curve of films obeyed the single-oscillator model.

Acknowledgements

This work was supported by Anadolu University Commission of Scientific Research Projects under Grant No. 061039, 081029 and 1001F05.

References

[1] C. Yan, L. Nikolova, A. Dadvand, C. Harnagea, A. Sarkissian, D.F. Perepichka, D. Xue, F. Rosei, Adv. Mater. 22 (2010) 1741.
[2] C. Yan, A. Dadvand, F. Rosei, D.F. Perepichka, J. Am. Chem. Soc. 132 (2010) 8868.
[3] M. Joseph, H. Tabata, T. Kawai, Jpn. J. Appl. Phys. Part 2 38 (1999) L1205.
[4] J.M. Bian, X.M. Li, X.D. Gao, W.D. Yu, L.D. Chen, Appl. Phys. Lett. 84 (2004) 541.
[5] M.G. Wardle, J.P. Goss, P.R. Briddon, Phys. Rev. B 71 (2005) 155205.
[6] A.S. Risbud, N.A. Spaldin, Z.Q. Chen, S. Stemmer, R. Seshadri, Phys. Rev. B 68 (2003) 205202.
[7] H.C. Jae, T. Hitoshi, K. Tomoji, J. Cryst. Growth 226 (2001) 493.
[8] J. Zhai, L. Zhang, X. Yao, Ceram. Int. 26 (2000) 883.
[9] F. Shinobu, S. Chikako, K. Toshio, Appl. Surf. Sci. 180 (2001) 341.
[10] M. Caglar, S. Ilican, Y. Caglar, F. Yakuphanoglu, Appl. Surf. Sci. 255 (2009) 4491.
[11] J.G. Lu, Z.Z. Ye, F. Zhuge, Y.J. Zeng, B.H. Zhao, L.P. Zhu, Appl. Phys. Lett. 85 (2004) 3134.
[12] S. Fujihara, C. Sasaki, T. Kimura, J. Eur. Ceram. Soc. 21 (2001) 2109.
[13] J. Liu, W. Weng, W. Ding, K. Cheng, P. Du, G. Shen, G. Han, Surf. Coat. Technol. 198 (2005) 274.
[14] X.W. Zhu, Y.Q. Li, Y. Lu, L.C. Liu, Y.B. Xia, Mater. Chem. Phys. 102 (2007) 75.
[15] L. Chen, Z. Ye, S. Lin, H. He, Y. Zeng, B. Zhao, L. Zhu, Mater. Lett. 62 (2008) 2554.
[16] M. Yu, H. Qiu, X. Chen, H. Li, W. Gong, Mater. Chem. Phys. 126 (2011) 797.
[17] X. Wang, L. Zhu, L. Zhang, J. Jiang, Z. Yang, Z. Ye, B. He, J. Alloys Compd. 509 (2011) 3282.
[18] S. Shet, K-S. Ahn, T. Deutsch, H. Wang, R. Nuggehalli, Y. Yan, J. Turner, M. Al-Jassim, J. Power Sources 195 (2010) 5801.
[19] S. Shet, K.-S. Ahn, H. Wang, R. Nuggehalli, Y. Yan, J. Turner, M. Al-Jassim, J. Mater. Sci. 45 (2010) 5218.
[20] M. Yu, H. Qiu, X. Chen, Thin Solid Films 518 (2010) 7174.
[21] S. Ilican, Y. Caglar, M. Caglar, F. Yakuphanoglu, Appl. Surf. Sci. 255 (2008) 2353.
[22] S. Ilican, M. Caglar, Y. Caglar, Appl. Surf. Sci. 256 (2010) 7204.
[23] Y. Caglar, S. Ilican, M. Caglar, F. Yakuphanoglu, J. Sol–Gel Sci. Technol. 53 (2010) 372.
[24] F. Yakuphanoglu, S. Ilican, M. Caglar, Y. Caglar, Superlattices Microstruct. 47 (2010) 732.
[25] M. Caglar, Y. Caglar, S. Aksoy, S. Ilican, Appl. Surf. Sci. 256 (2010) 4966.
[26] C.S. Barret, T.B. Massalski, Structure of Metals, Pergamon Press, Oxford, 1980.
[27] A. Khorsand Zak, W.H. Abd. Majid, M.E. Abrishami, R. Yousefi, Solid State Sci. 13 (2011) 251.
[28] B.D. Cullity, S.R. Stock, Elements of X-ray Diffraction, 3rd ed., Prentice Hall, 2001.
[29] M. Birkholz, Thin Film Analysis by X-ray Scattering, Wiley-VCH Verlag GmbH and Co. KGaA, Weinheim, 2006.
[30] Z.G. Wang, X.T. Zu, S. Zhu, L.M. Wang, Physica E 35 (2006) 199.
[31] P.T. Hsieh, Y.C. Chen, K.S. Kao, C.M. Wang, Appl. Phys. A 90 (2008) 317.
[32] M. Chen, X. Wang, Y.H. Yu, Z.L. Pei, X.D. Bai, C. Sun, R.F. Huang, L.S. Wen, Appl. Surf. Sci. 158 (2000) 134.
[33] M. Sano, T. Adaniya, T. Fujitani, J. Nakamura, Surf. Sci. 514 (2002) 261.
[34] Y. Jin, Q. Cui, G. Wen, Q. Wang, J. Hao, S. Wang, J. Zhang, J. Phys. D: Appl. Phys. 42 (2009) 215007.
[35] C.D. Wanger, W.M. Riggs, L.E. Davis, J.F. Moulder, G.E. Muilenberg, Handb. X-Ray Photoelectron Spectrosc. (1979).
[36] S. Diplas, P. Tsakiropoulos, R.M.D. Brydson, J.F. Watts, Philos. Mag. A 77 (4) (1998) 1067.
[37] B. Wang, L. Tang, J. Qi, H. Du, Z. Zhang, J. Alloys Compd. 503 (2010) 436.
[38] J.I. Pankove, Optical Processes in Semiconductors, Prentice-Hall Inc., Englewood Cliffs, NJ, 1971.
[39] N. Veissid, C.Y. An, A. Ferreira da Silva, J.I. Pinto de Souza, Mater. Res. 2 (1999) 279.
[40] G.D. Cody, J. Non-Cryst. Solids 141 (1992) 3.
[41] F. Urbach, Phys. Rev. 92 (1953) 1324.
[42] M. Caglar, S. Ilican, Y. Caglar, Thin Solid Films 517 (2009) 5023.
[43] J. Tauc, Amorphous and Liquid Semiconductors, Plenum Press, New York, 1974.
[44] F. Yakuphanoglu, A. Cukurovali, I. Yilmaz, Opt. Mater. 27 (2005) 1363.
[45] F. Abeles (Ed.), Optical Properties of Solids, North-Holland, Publishing Company, London, UK, 1972.
[46] M. DiDomenico, S.H. Wemple, J. Appl. Phys. 40 (1969) 720.
[47] F. Karipcin, E. Kabalcilar, S. Ilican, Y. Caglar, M. Caglar, Spectrochim. Acta A 73 (2009) 174.
[48] M. Caglar, S. Ilican, Y. Caglar, Opt. Commun. 281 (2008) 1615.
[49] S.H. Wemple, M. DiDomenico, Phys. Rev. B 3 (1971) 1338.
[50] A. Abdolahzadeh Ziabari, F.E. Ghodsi, J. Alloys Compd. 509 (2011) 8748.
[51] D.K. Madhup, D.P. Subedi, A. Huczko, Optoelectron. Adv. Mater. 4 (2010) 1582.
[52] S.H. Wemple, M. Didomenico, Phys. Rev. B 3 (1971) 1338.